Solvothermal synthesis of surfactant free spherical nickel hydroxide/graphene oxide composite for supercapacitor application

A.A. Khaleed[a], A. Bello[a], J. K. Dangbegnon[a], M.J. Madito[a], O. Olaniyan[a], F. Barzegar[a], K. Makgopa[c], , K.O. Oyedotun[a], B. W. Mwakikunga[b], S. C. Ray[d], N. Manyala[a],*

[a] Department of Physics, Institute of Applied Materials, SARCHI Chair in Carbon Technology and Materials, University of Pretoria, Pretoria 0028, South Africa

[b] DST/CSIR National Centre for Nano Structured Materials ,Council for Scientific and Industrial Research, P.O. Box 395, Pretoria 0001, South Africa

[c]Department of Chemistry, University of Pretoria, Pretoria 0002, South Africa

[d]Department of Physics, University of South Africa, Pretoria 0002, South Africa

*Corresponding author: N. Manyala (Ncholu.Manyala@up.ac.za)

Highlights

- Use of solvothermal technique for production of nickel hydroxide/graphene oxide composite.
- Spherical nickel hydroxide composed of nanosheets.
- Excellent electrochemical properties of composite electrode material.

Abstract

Spherical composite of $Ni(OH)_2$/GO was produced via a surfactant free solvothermal technique and tested as electrode materials for electrochemical capacitors. The structural and morphological analysis confirmed that deposition of $Ni(OH)_2$ onto GO does not change the crystal structure of pure hexagonal α-$Ni(OH)_2$. Electrode fabricated from the $Ni(OH)_2$/GO composite demonstrates a superior electrochemical performance when compared to that of pure $Ni(OH)_2$, GO, and Mix-$Ni(OH)_2$/GO electrodes with $Ni(OH)_2$/GO electrode exhibiting a specific capacity of ~420 mA h g^{-1} which correspond to a specific capacitance of 3619 F g^{-1} at 2.5 A g^{-1}, as well as a corresponding rate capability of 78% at 10 A g^{-1}. The stability study of the

$Ni(OH)_2$/GO composite reveals a good capacity retention of ~95% at a current density of 10 A g^{-1} after 3000 charge-discharge cycles.

Keywords: α-$Ni(OH)_2$, graphene oxide, nanocomposite, supercapacitor

Introduction

The growing need for energy coupled with the rise in global warming and air pollution due to the burning and consumption of fossil fuels has led to an increase in alternative energy sources to meet the exponential rise in energy demand [1–3]. These alternative energy sources often require a storage device as the energy production is not constant throughout the days and nights. Electrochemical capacitors (ECs) also known as supercapacitors (SCs) have attracted great attention in electrochemical energy storage application owing to their outstanding work rate, excellent cycle life and high power density [4,5]. In general, they are classified into two classes based on the mechanism in which they store charges: Electrochemical double-layer capacitors (EDLCs) which store energy based on ion adsorption, and faradaic capacitor which store energy by the fast surface redox process [6,7].

$Ni(OH)_2$, among many faradaic electrode materials has being considered as a potential electrode material due to its low cost, low toxicity, and high theoretical specific capacity (433 $mA{\cdot}hg^{-1}$)[6,8,9]. Nonetheless, $Ni(OH)_2$ suffers from low electrical conductivity, low rate capability and poor cycling stability, which affect its electrochemical performance and hence, restrict its commercialization [10].

Carbon nanomaterials such as graphene oxide (GO), carbon nanotubes (CNT) have been established to be effective in improving the electrochemical performance of $Ni(OH)_2$-based electrode materials when used as a supporting material [8,11,12]. GO, known as an intermediary product in the preparation of graphene, has been studied as a feasible electrode material for SCs [13–15]. The ease at which GO can be prepared in a considerable amount via a modified Hummer's method, with a high specific surface area, and high oxygen-containing functional groups are the main attractions of GO as an active material for electrochemical applications [13,15,16]. Many $Ni(OH)_2$ composite materials with GO have been reported, for example, Ma *et al.* reported a β-$Ni(OH)_2$/GO/CNTs composite with a specific capacitance (C_{sp}) of ∼1815 F g^{-1} at 2 A g^{-1} and capacitance retention of ∼97% at 10 A g^{-1} after 2000 cycles [14].Wang *et al.* investigated the electrochemical performance of $Ni(OH)_2$ nanoparticles deposited on GO and reported a C_{sp} of ∼ 440 F g^{-1}at 2.8 A g^{-1}[17]. Mao *et al.* used 3D nitrogen-containing GO hydrogel substrate for the in-situ growth of $Ni(OH)_2$ nanoplates via an adsorption-hydrothermal strategy, the composite was reported to have a C_{sp} of 1748 F g^{-1} at 0.2 A g^{-1} [18]. Chen *et al.* reported a C_{sp} of ∼1160 F g^{-1} at 5 A g^{-1} for a $Ni(OH)_2$-GO hydrogel prepared using hydrothermal procedure [19]. However, the above reported works on $Ni(OH)_2$ composite with GO have limitations in their electrochemical performances such as rate capabilities and specific capacitance values which is far below the reported theoretical specific capacitance of $Ni(OH)_2$. Hence, the need to exploit more synthesis techniques in order to optimize the electrochemical performances of $Ni(OH)_2$/GO based composites is imperative.

Herein, we successfully prepared $Ni(OH)_2$/GO composite using surfactant-free solvothermal technique and investigated its electrochemical properties. The choice of surfactant-free

synthesis is to avoid contamination caused by the use of the surfactant or templates often observed in the products, affecting various applications of the synthesized materials. The $Ni(OH)_2$/GO electrode displays superior electrochemical performance as compared with pure $Ni(OH)_2$ with a specific capacity of ~ 420 $mAhg^{-1}$ corresponding to specific capacitance of 3619 F g^{-1} at 2.5 A g^{-1}, and good capacity retention of ~ 95 % after 3000 cycles at 10 A g^{-1}.

Experimental

Synthesis of GO

GO was prepared by the modification of the established Hummer's method from graphite powder. Briefly, 5.0 g of graphite powder was poured into a round bottom flask containing 15 mL of concentrated H_2SO_4, followed by stirring and the addition of fuming HNO_3 and continuous stirring of the mixture at room temperature for 24 h. Subsequently, the mixture was centrifuged four times, washed with deionized water and dried in an electric oven for 24 h at 60 °C to obtain a graphite intercalation compound powder (GICP). Thermal expansion of the GICP to expanded graphite (EG) was achieved after heating the GICP at 1050 °C for 15 s. Finally, 1.0 g of EG (a precursor for GO) was dissolved in a 200 mL of concentrated H_2SO_4 in a 500 mL three-necked flask, followed by slow addition of 10 g $KMnO_4$ and transferring the mixture into an ice bath, and slow addition of 200 mL of deionized water and 50 mL H_2O_2. The mixture was then stirred for 30 min, resulting in a light brown suspension of GO. The obtained sample of GO was washed with an aqueous HCl in a ratio 9:1 of water:HCl, followed by continuous centrifugation and washing with deionized water until pH of about 7 was achieved, then dried at 80 °C for 12 h [20,21].

Synthesis of α-$Ni(OH)_2$/GO

2.33 g of $Ni(NO_3).6H_2O$ was dissolved in 40 mL of N, N-dimethylformamide (DMF) at room temperature under magnetic stirring, followed by the addition of 50 mg of GO and sonication for 1 h to get a uniform dispersion of GO in the solution. The solution was transferred into a 60 mL Teflon-lined autoclave and sealed. The autoclave was then placed into an electrical oven preheated at 180 °C and kept at that temperature for 18 h. Subsequently, the sample was removed from the oven and allowed to cool down to room temperature naturally. The obtained black powder was washed with deionized water until pH 7 was achieved and then dried at 60 °C overnight. A ratio of 9:1 of $Ni(OH)_2$ and GO in the composite is obtained based on the approximated final mass of the composite (500 mg). For comparison, Pure $Ni(OH)_2$ was synthesized via the same procedure with no addition of GO. In order to investigate the effect of solvothermal synthesis, 77.4 mg $Ni(OH)_2$ and 2.6 mg GO were physically mixed in an agate mortar using pestle to obtained Mix-$Ni(OH)_2$/GO.

Characterization and electrode fabrication

Powder X-ray diffraction technique (XRD) in a θ/2θ pattern, with a cobalt tube at 50 mA and 35 kV (XPERT-PRO diffractometer, PANalytical BV, Netherlands) was employed to probe the crystallinity of the materials. Raman spectroscopic technique was employed to examine the vibrational mode of the samples utilizing a T64000 micro-Raman spectrometer, having a low power of 12 mW and an excitation wavelength 514 nm. X-ray photoelectron spectroscopy (XPS) measurements of the samples were conducted using a Physical Electronics VersaProbe 5000 spectrometer operating with a 100 µm monochromatic Al-Kα exciting source. A Zeiss Ultra Plus

55, field emission scanning electron microscopy (FESEM) operating at 2.0 kV was employed to examine the morphology of the samples. Electron micrograph and selected area diffraction patterns of the composite were collected using high-resolution transmission electron microscopy (HR-TEM) JEOL 2100 (from Tokyo Japan) equipped with LaB6 filament, a Gartan U1000 camera of 2028 x 2028 pixels and operated at 200 kV. The HR-TEM is equipped with an integrated scanning transmission electron microscopy along with energy dispersive X-ray (STEM-EDX). A Micromeritics TriStar II 3020 (version 2.00) analyzer was employed for the specific surface area (SSA) analysis of the samples using Brunauer–Emmett–Teller (BET) method from the adsorption branch in the relative pressure range (P/P_0) of 0.01 – 1. Thermogravimetric analysis (TGA) was carried out using a thermogravimetric analyzer (Hitachi TGA) from 20 °C to 1000 °C in air. A Bio-Logic VMP300 workstation (Knoxville TN 37,930, USA) in a three-electrode configuration was used to probe the electrochemical performance of the samples. This configuration consists of a working electrode (electrode material), reference electrode (Ag/AgCl (3 M KCl)) and counter electrode (glassy carbon) in a 6.0 M KOH aqueous electrolyte. The electrodes were prepared by mixing 80 wt% of the samples with 10 wt.% carbon black (to increase the conductivity of the electrode materials) and 10 wt.% polyvinylidene difluoride (PVdF) as a binder in an agate mortar. This was followed by dissolving the mixture in the 1-methyl-2-pyrrolidinone (NMP) to form a homogenous paste. The paste was then smeared on a Ni foam current collector and dried in an electrical oven for 8 h at 60 °C to ensure complete evaporation of the NMP. The mass of the electrode materials ranged from 2.1 - 2.3 mg. Subsequently, Cyclic voltammetry (CV) probed at a potential window of 0 - 0.5 V (vs. Ag/AgCl, 3 M KCl) potential window was carried out at different scan rates from 5 to 50 mV s^{-1}. The

galvanostatic charge–discharge (CD) measurement was performed at current densities from 2.5 to 10 A g^{-1} and an open circuit with a frequency range of 10 mHz–100 kHz were employed for the electrochemical impedance spectroscopy (EIS) measurement.

Results

Structural and morphological properties

The cobalt source (Co-K_α) with a wavelength of 0.17890 nm was used for the XRD analysis of the samples. The diffraction patterns of the samples are illustrated in Fig. 1a. Four peaks relating to the crystallographic planes of (003), (006), (101), (111) and (110) are observed in $Ni(OH)_2$ (Fig. 1a). This describes a hexagonal configuration of single phase α-$Ni(OH)_2$ (JCPD NO. 38-0715). Moreover, in addition to the α-$Ni(OH)_2$ diffraction patterns, a weak peak at 12.1° corresponding to the (001) plane of GO appears in the $Ni(OH)_2$/GO sample, corroborating the existence of GO in the sample. The observed small shift in the 2θ value positions of the crystallographic planes of both $Ni(OH)_2$ and GO is as a result of the difference in wavelength of Co and Cu excitation sources. Co has longer wavelength, therefore it will result to crystallographic plane at higher 2θ value position [4].

Fig. 1b presents the Raman spectra of GO, $Ni(OH)_2$ and $Ni(OH)_2$/GO. The Raman spectrum of GO reveals a D-band at ~1352 cm^{-1} ascribed to the disorder-induced vibration as a result of structural defects. An intensive G-band at ~1584 cm^{-1} is attributed to the first-order scattering of the E_{2g} vibrational mode and 2D-band at ~2705 cm^{-1} corresponding to the second-order two-phonon vibration of D [22].The intensity ratio of G/D is found to be 1.4 which confirms the good quality of our GO. In the Raman spectrum of $Ni(OH)_2$ peaks at ~355 cm^{-1} could be related to the

E_U(T) vibrational mode, 512 cm^{-1} corresponds to the 2nd order acoustic mode resulting from harmonic overtone of an acoustic vibration at ~250–270 cm^{-1}, 686 cm^{-1} corresponds to $2E_g$ transition due to the harmonic overtone at 306–318 cm^{-1}, 724 cm^{-1} could be ascribed to $2E_g$ O-H bend and 1050 cm^{-1} could be assigned to v_1 2nd order lattice mode [23,24]. Moreover, the Raman spectrum of $Ni(OH)_2$/GO composite revealed the D-band (~1352 cm^{-1}), the G-band (1585 cm^{-1}) and the 2D-band (~2705 cm^{-1}) of graphene oxide, in addition to the 350, 512, 686, 724 and 1049 cm^{-1} of $Ni(OH)_2$. Hence, the Raman peaks coming from GO are still maintained in the composite.

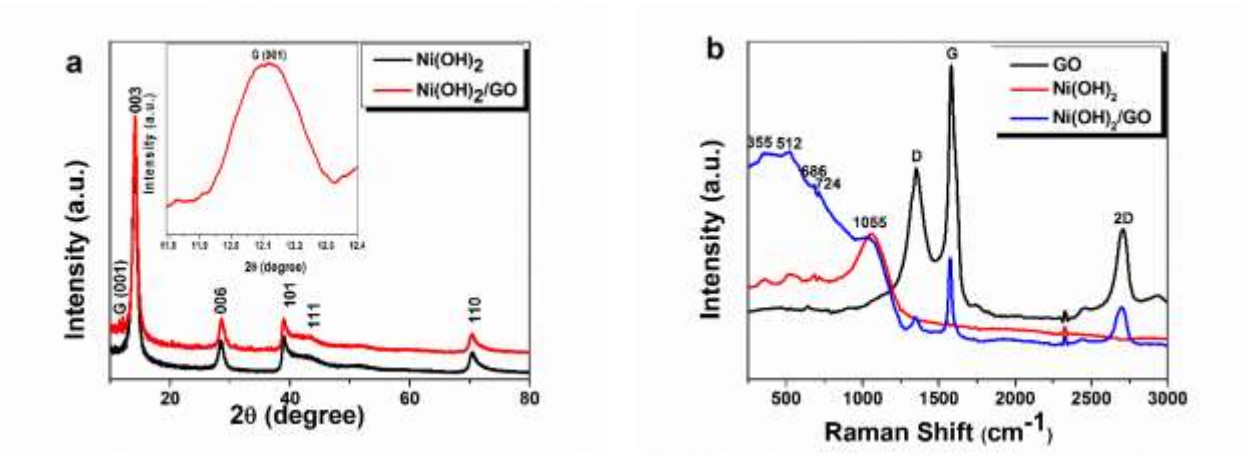

Fig. 1. (a) XRD spectra of $Ni(OH)_2$ and $Ni(OH)_2$/GO composite (inset to the figure is a (001) plane of GO), (b) Raman spectra of GO, $Ni(OH)_2$ and $Ni(OH)_2$/GO composite.

The surface chemistry of the samples was analyzed by XPS. Fig. 2a shows the wide scan XPS spectrum of the as-received (i.e., without sputter cleaning) $Ni(OH)_2$/GO composite, which displays the main elements (12.01 at% Ni 2p, 46.71 at% O 1s and 41.29 at% C 1s) of the composition of the sample. The core level spectrum of Ni 2p of a composite sample reveals the binding energy peaks at 853.2, 857.5, 862.8, 870.7, 875.2 and 880.4 eV which agree with Ni

$2p_{3/2}$ and Ni $2p_{1/2}$, assigned to the characteristic of N^0, Ni^{2+} and Ni^{3+} and the two shakeup satellite [25,26], as shown in Fig. 2b. The core level spectrum of Ni 2p suggests that the composite sample has a noticeable amount of metallic nickel (Ni^0 at 853.2 eV), usually reported around 852.6 eV [27]. The Ni 2p components at high binding energies are assigned to Ni^{2+} bound to O and OH groups in $Ni(OH)_2$ and NiO, and Ni^{3+} in NiOOH [27]. Fig. 2c shows the core level spectrum of C 1s of a composite sample which reveals the binding energy peaks at 282.2, 284.5, 285.5, 287.6 and 290.3 eV corresponding to –COOH, sp^2 C=C/C−C (graphene/graphite component), C−O, C=O and O−C=O (oxide components/functional groups), respectively [28–30]. The $Ni(OH)_2$/GO composite sample shows much higher composition of hydroxyl and epoxy, carbonyl and carboxyl functional groups. Fig. 2d shows the core level spectrum of O 1s with fitted peaks at 528.5, 530.2 and 533.1 eV which could be ascribed to metal–oxygen bonds, oxygen in OH^- groups and GO [31]. Furthermore, Fig. 1e shows the wide scan XPS spectrum of the as-received GO sample, which displays 54.86 at% O 1s and 45.14 at% C 1s. This wide scan spectrum clearly shows that GO used for composite synthesis has high purity as it shows no traces of impurities. The GO sample shows atomic percentage ratio of 0.82 for C 1s/O 1s, while $Ni(OH)_2$/GO composite sample shows a ratio of 0.88, as obtained from the wide scan spectra of both samples. The C 1s/O 1s ratio values obtained from both samples are equivalent suggesting no loss in materials; GO in particular, during solvothermal synthesis. Fig. 2f shows the core level spectrum of C 1s of a GO sample. The fitted binding energy peaks 284.2, 286.5 and 288.3 eV correspond to sp^2 C=C/C−C, C−O and C=O, respectively [28,29]. The GO sample and the $Ni(OH)_2$/GO composite sample show equivalent percentage of hydroxyl and epoxy (C−O), and carbonyl (C=O) groups. However, the GO sample shows higher carbon content (C=C/C−C) which

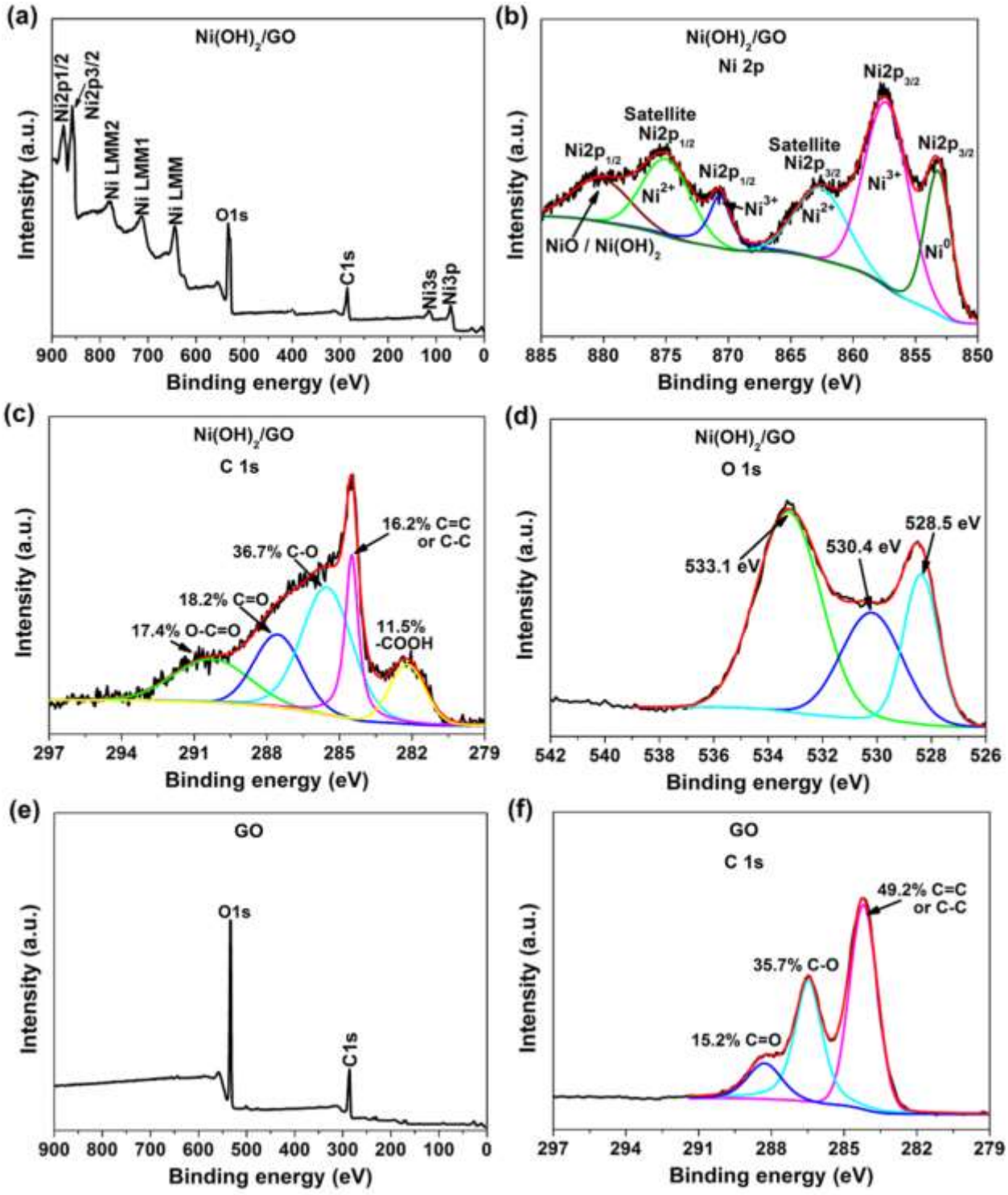

Fig 2. XPS data : (a) The wide scan spectra of the as-received (i.e. without sputter cleaning) $Ni(OH)_2$/GO composite, the core level spectrum of (b) Ni 2p, (c) C 1s and (d) O 1s of a composite sample, (e) The wide scan spectra of the GO and (f) the core level spectrum of C 1s.

mostly reacted with oxygen from $Ni(OH)_2$ to yield additional oxide components as seen in Fig. 2c for $Ni(OH)_2$/GO composite sample. It is noted that a $Ni(OH)_2$/GO composite sample does not reveal obvious solvothermal reduction of GO in the composite as it shows high percentage of functional groups, in fact, a reduced GO would show a much higher percentage of carbon and much lower percentage of functional groups [30].

Fig. 3a and 3b illustrate low and high magnification micrographs of $Ni(OH)_2$. Spherical nanosheets were observed for the pure $Ni(OH)_2$. The formation of the spheres could be elucidated from the dissolution of the $Ni(NO_3).6H_2O$ to form Ni^{2+} ion in the solution, the water molecules from hydrate $Ni(NO_3).6H_2O$ become free and supply OH^- ions for the growth of thin $Ni(OH)_2$ nanosheets. As the reaction proceed, thin nanosheets of $Ni(OH)_2$ self-assembled through the process of Ostwald ripening to form spheres in order to minimize the surface energy of the thin $Ni(OH)_2$nanosheets[32,33].Coalescence mechanism, an oriented attachment mechanism, plays a vital role in the Oswald-ripening process [32,34]. Fig. 3c and 3d represent the low and high magnifications micrographs of GO. The figures showed that GO was well exfoliated to develop broken thin sheets and wrinkles to establish the GO structures. $Ni(OH)_2$ grown on the surface of the GO sheets are revealed at low magnification (Fig. 3e). Whereas the high magnification of $Ni(OH)_2$/GO confirmed the composite maintained the structure of pure $Ni(OH)_2$ (Fig 3f).

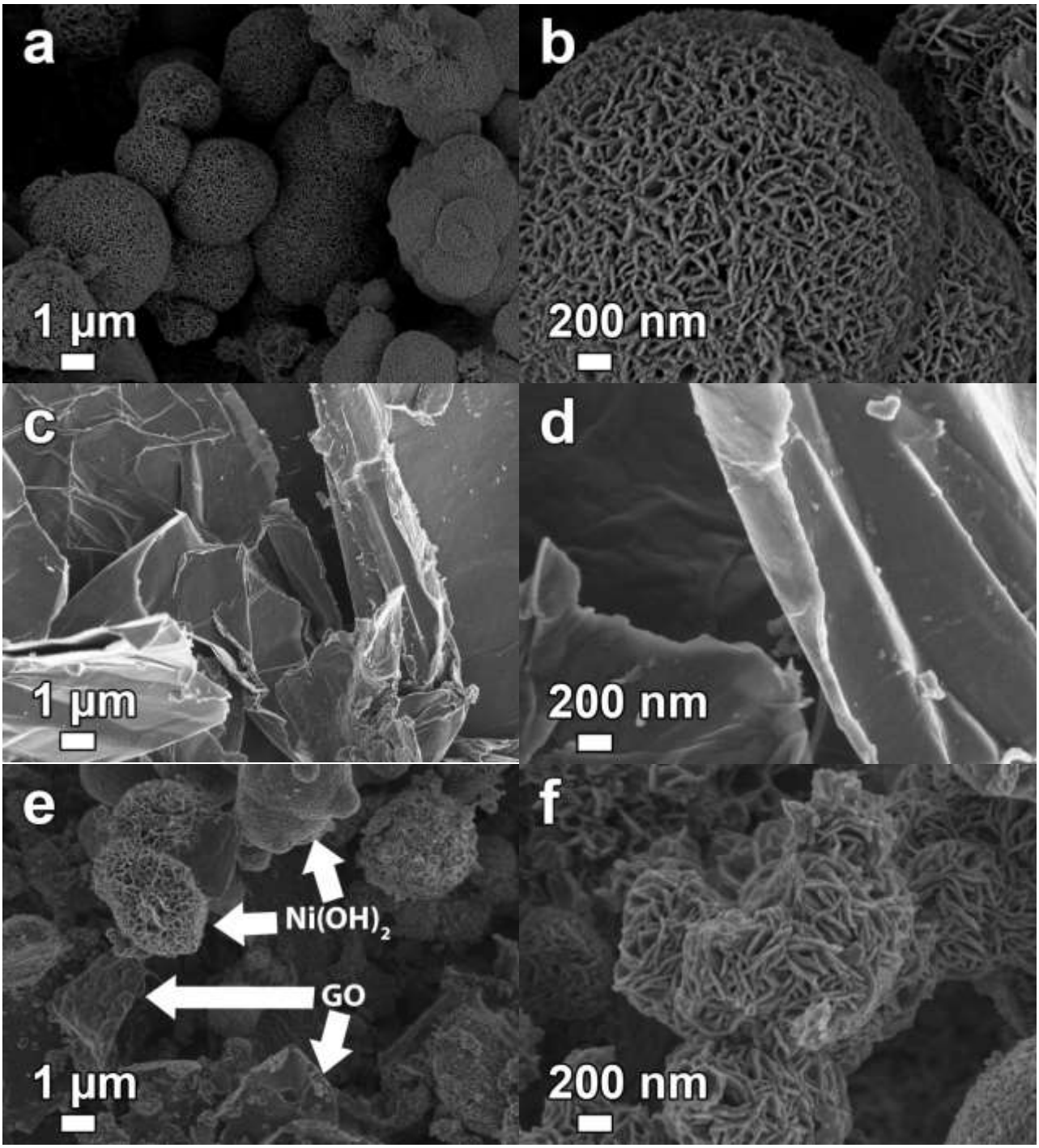

Fig. 3. SEM micrographs: (a) and (b) low and high magnification of the $Ni(OH)_2$, (c) and (d) low and high magnification of the GO, (e) and (f) low and high magnification of the $Ni(OH)_2$/GO.

To obtain information on the thickness of the GO HRTEM was used as shown in Fig. 4. Fig. 4a shows the HRTEM micrograph of GO with the folded area showing fringes (see inset to the

figure) corresponding to four layers of graphene which display a distinctively selected area electron diffraction pattern (SAED) of a few-layer graphene, as shown in Fig. 4b. In addition, Fig. 4c shows the diffraction intensity profile of a SAED pattern in Fig. 4b which suggest that the evaluated GO area has four stacked layers of graphene with an interlayer spacing of about 0.43 nm. This suggests that a GO used in this study has few layers of functionalized graphene.

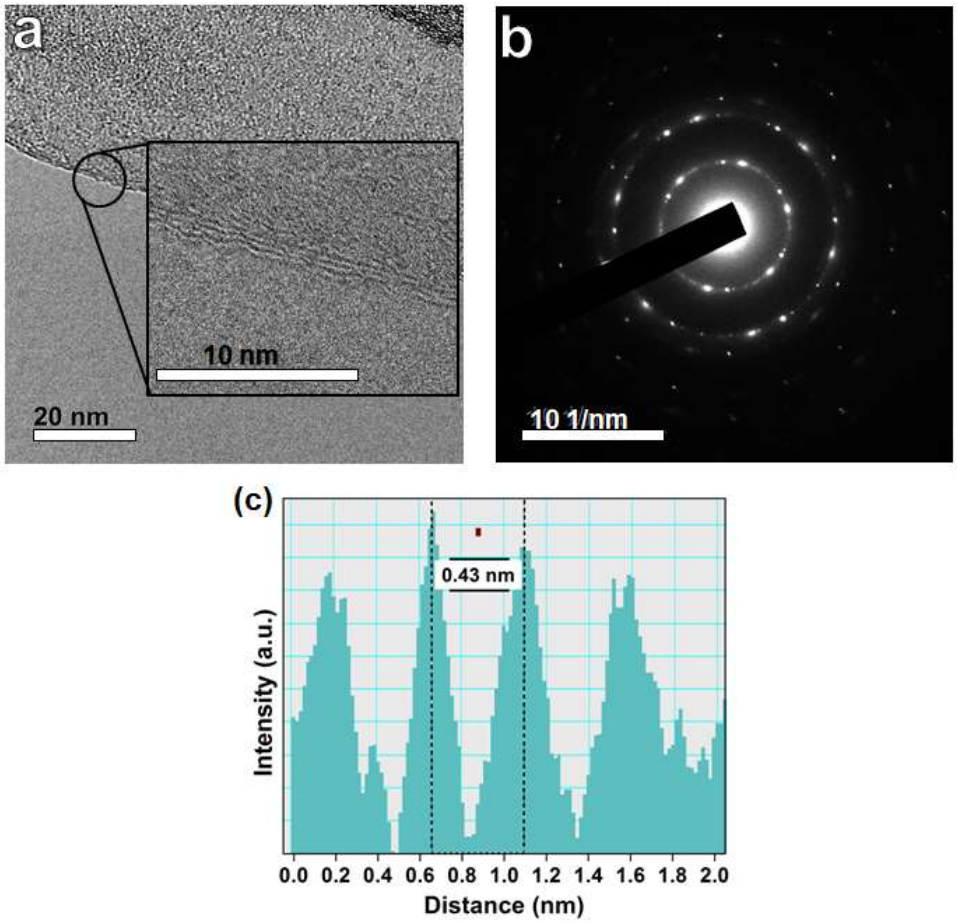

Fig 4. (a) HRTEM micrograph of GO (inset to the figure display higher magnification HRTEM micrograph of GO taken from a region shown with a circle), (b) selected area electron diffraction pattern (SAED) taken from a region shown by inset to figure in (a), and (c) the corresponding SAED diffraction intensity profile.

To get information on the homogeneity or rather dispersion of $Ni(OH)_2$ on the GO in the composite material, the morphology of a composite was investigated using HRTEM and the

micrographs are displayed in Fig. 5. It can be seen from Fig. 5a and 5b that $Ni(OH)_2$ is mostly homogeneously dispersed in the GO matrix to form composite material. This was further compared to a Mix-$Ni(OH)_2$/GO sample which shows a poor or non-uniform dispersion of $Ni(OH)_2$ on the GO matrix, as shown in Fig. 5c.

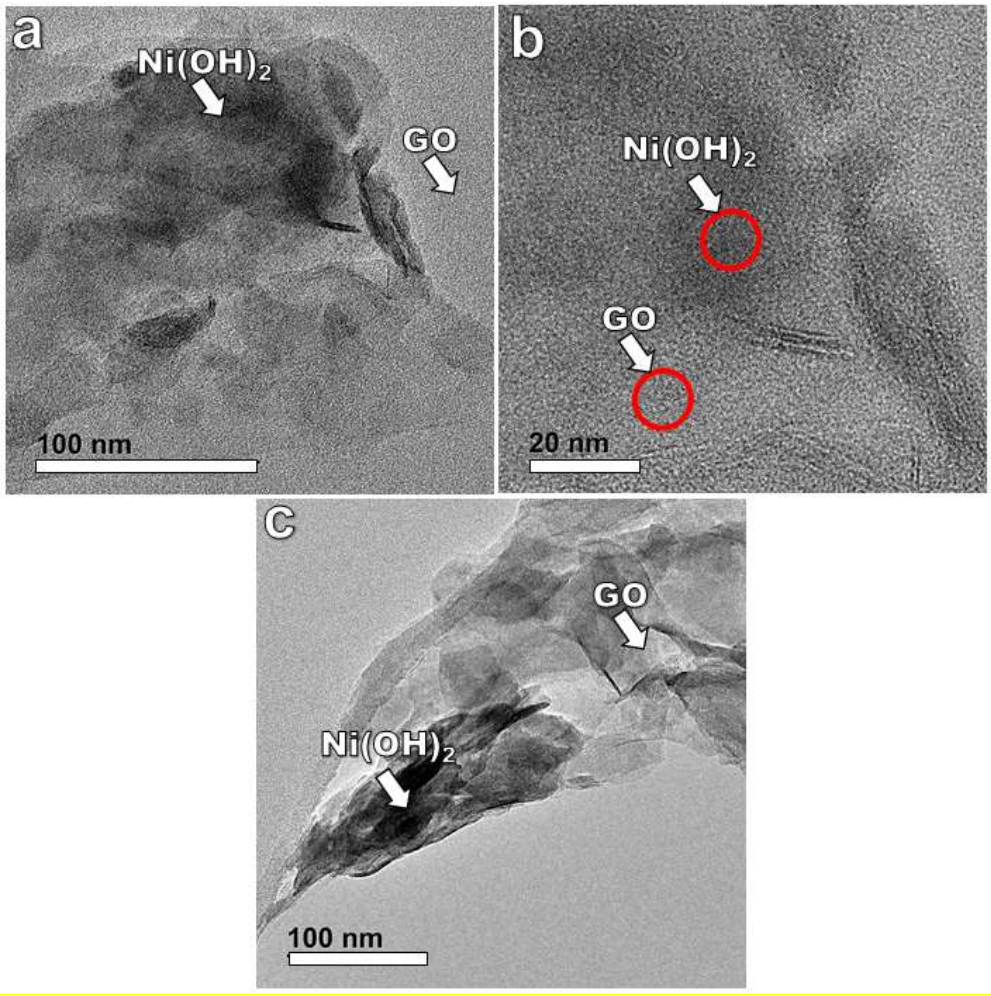

Fig 5. (a) and (b) HRTEM micrographs of $Ni(OH)_2$/GO composite sample at low and high magnification respectively. (c) An HRTEM micrograph of Mix-$Ni(OH)_2$/GO.

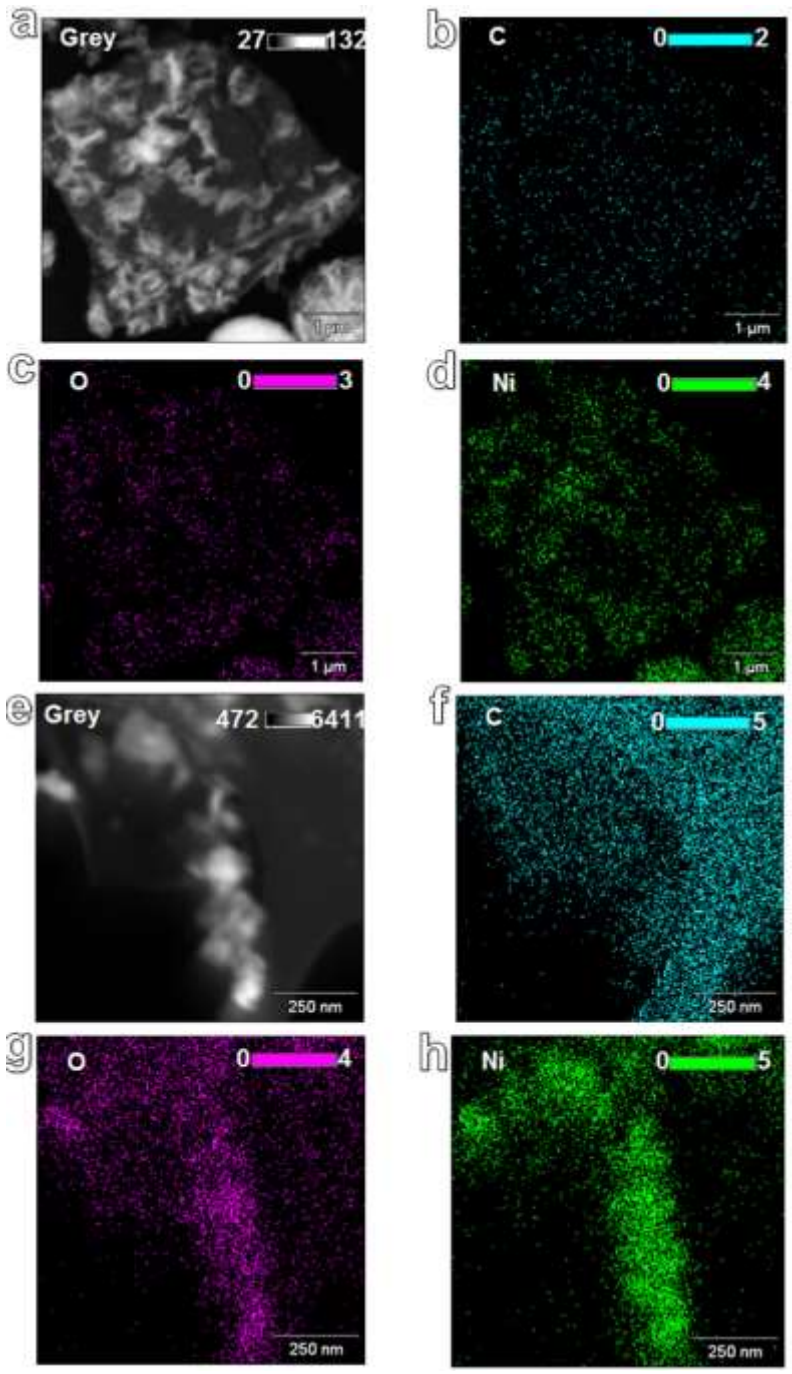

Fig 6. (a) A scanning transmission electron microscopy image and (b - d) the corresponding energy dispersive X-ray maps of C, O and Ni respectively of the $Ni(OH)_2$/GO sample. (e) A scanning transmission electron microscopy image and (f - h) the corresponding energy dispersive X-ray maps of C, O and Ni respectively of the Mix-$Ni(OH)_2$/GO sample.

To further evaluate the dispersion of $Ni(OH)_2$ on the GO in the composite material, the elemental mapping of a composite was obtained using a scanning transmission electron microscopy along with energy dispersive X-ray (STEM-EDX) and the maps are displayed in Fig. 6. Fig. 6a shows a scanning transmission electron microscopy image and Fig. 6b - d show the corresponding energy dispersive X-ray maps of C, O and Ni which are main elements of the composition of $Ni(OH)_2$/GO sample. These maps clearly reveal a homogeneous distribution of the evaluated main elements of the $Ni(OH)_2$/GO sample suggesting that the dispersion of $Ni(OH)_2$ on the GO matrix in the composite material is uniform, in accordance with the HRTEM micrographs of $Ni(OH)_2$/GO composite. In contrast to $Ni(OH)_2$/GO sample, a Mix-$Ni(OH)_2$/GO sample shows a non-homogeneous distribution of the evaluated main elements suggesting that the dispersion of $Ni(OH)_2$ on the GO matrix in the sample is non-uniform (Fig. 6e-h), also in accordance with the HRTEM micrographs of Mix-$Ni(OH)_2$/GO sample.

The BET SSA is a vital parameter used to evaluate the suitability of the material for SCs application. Hence, this parameter was investigated using Nitrogen physisorption and the result is displayed in Fig. 7a. The adsorption-desorption isotherm plots for both samples presented in the figure exhibited a type III isotherms with H4 hysteresis revealing complex materials containing mesopores. The BET SSA measured based on the BET method are 51.2 m^2/g and 71.0 m^2/g for $Ni(OH)_2$ and $Ni(OH)_2$/GO, respectively. Fig. 7b shows the pore size distribution (PSD) curves of the samples, the samples are observed to have similar average pore size of $\sim$3 nm, signifying that they consist of a mesoporous structures. Compared with the SSA value of $Ni(OH)_2$, the higher surface area of $Ni(OH)_2$/GO composite could be credited to the addition of GO into spherical $Ni(OH)_2$ nanosheets.

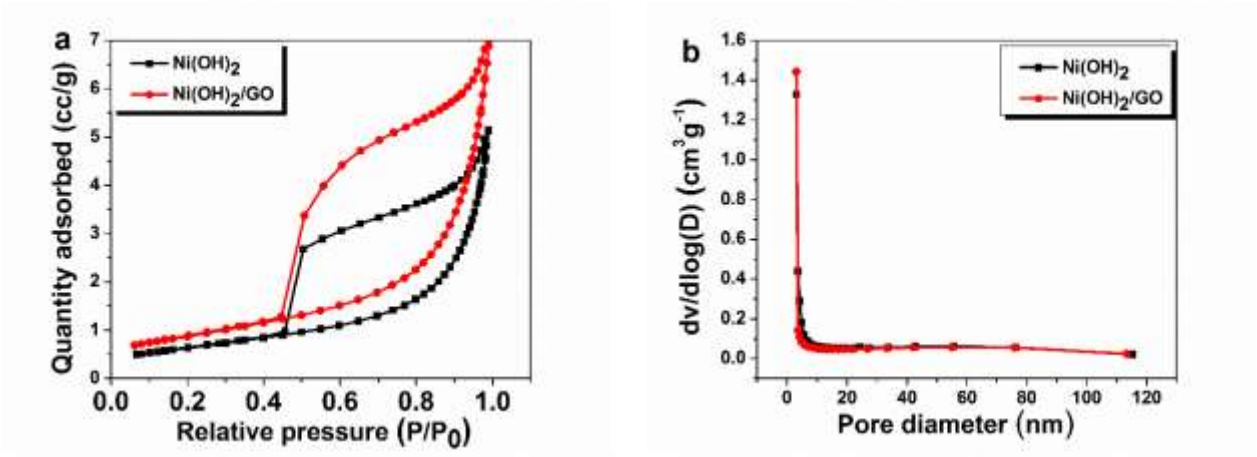

Fig. 7. (a) N_2 adsorption-desorption isotherm linear plots of $Ni(OH)_2$ and $Ni(OH)_2$/GO and (b) Pore size distribution curves obtained from BJH method.

The GO content of the Ni(OH)2/GO sample can be determined from the TGA analysis. Figure 8 presents TGA curves of $Ni(OH)_2$ and $Ni(OH)_2$/GO samples. From the curves, the weight loss under 100 °C corresponds to the loss of any interfacial-adsorbed water molecules in both $Ni(OH)_2$ and $Ni(OH)_2$/GO samples. Below 230 °C, the two samples exhibit a slight weight loss due to the evaporation of adsorbed water molecules [5]. Moreover, $Ni(OH)_2$ displays a substantial weight loss between 240−300 °C, coming from the transformation of $Ni(OH)_2$ to NiO [5]. Whereas, the considerable weight loss from 240 °C to 400 °C in the $Ni(OH)_2$/GO sample is related to both decomposition of $Ni(OH)_2$ to NiO and combustion of the GO [5]. The GO content was calculated to be 3.29% based on the residual weights of the two samples at 100 °C.

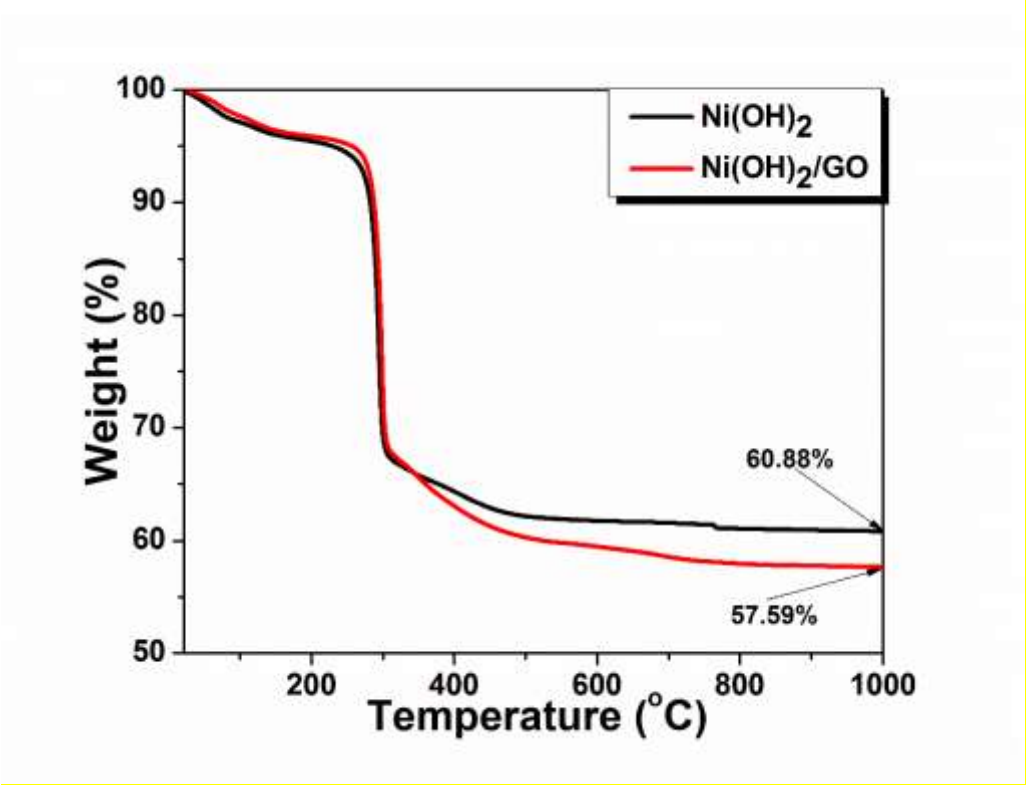

Fig. 8 TG curves of $Ni(OH)_2$ and $Ni(OH)_2$/GO samples

Electrochemical properties

Fig. 9a showed the CV curves of pure $Ni(OH)_2$, GO, $Ni(OH)_2$/GO and Mix-Ni(OH)2/GO electrodes at a scan rate of 10 mV s^{-1} within the potential range of 0 - 0.5 V (vs. Ag/AgCl). The curves revealed a pair of redox peaks, implying their predictable faradaic-capacity characteristics. The presence of redox peaks in GO electrode CV curve could be attributed to the ongoing electrochemical redox reactions arising from the high presence of oxygen functionalities that have high redox reactivity characteristics in the positive potential window [35,36]. Whereas, the anodic and cathodic peaks present in $Ni(OH)_2$-based electrodes emanated from the oxidation and reduction reactions of $Ni(OH)_2$ to NiOOH, respectively as shown [4,37]:

$$Ni(OH)_2 + OH^- \longleftrightarrow NiOOH + H_2O + e^- \quad (1)$$

The larger current density observed in the CV of the $Ni(OH)_2$/GO electrode compared to that of $Ni(OH)_2$, GO, and Mix-Ni(OH)2/GO electrodes in Fig. 9a, signifies an enhanced specific capacity [38]. This could be attributed to the synergy between spherical $Ni(OH)_2$ and GO, which inhibits the restacking of the GO sheet, therefore affording larger surface area for better accessibility of electrolyte ion (OH^-), as well as abundant oxygen-containing groups (epoxy, alkoxy) in the composite providing additional capacity and increased in wettability [39]. Fig 9b-e displayed cyclic voltammograms of pure $Ni(OH)_2$, GO, $Ni(OH)_2$/GO and Mix-Ni(OH)2/GO electrodes at scan rates from 5 to 50 mV s^{-1}. The figures indicated that with increasing scan rate, the anodic and cathodic peaks potentials shift in the positive and negative direction, arising from the inadequacy of the rate of ion diffusion to gratify electronic neutralization in the redox process [40]. This also corroborates that the electrochemical reaction is diffusion controlled as for faradaic mechanism.

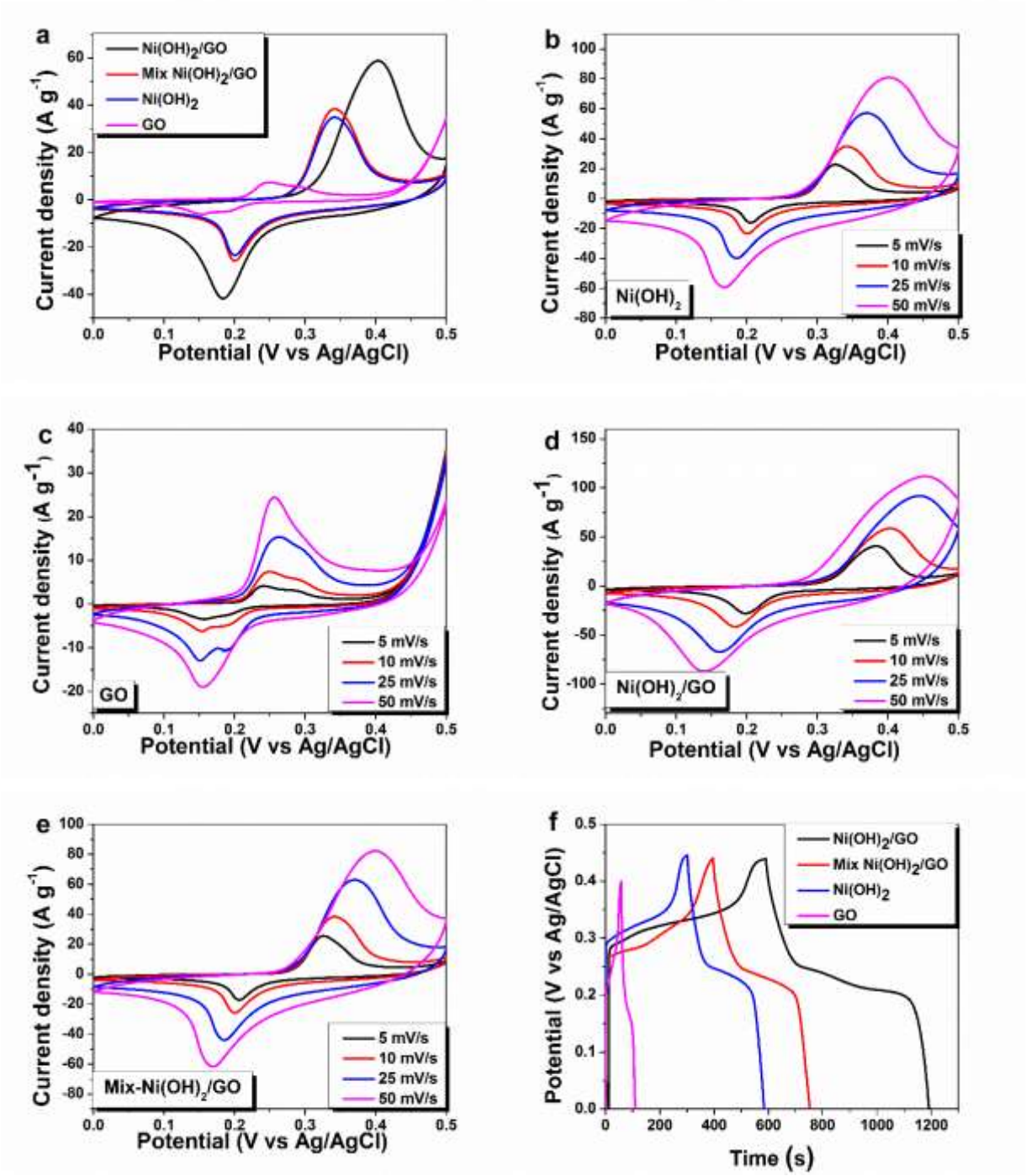
a
Ni(OH)2/GO
Mix Ni(OH)2/GO
Ni(OH)2
GO
Current density (A g-1)
Potential (V vs Ag/AgCl)
b
Ni(OH)2
5 mV/s
10 mV/s
25 mV/s
50 mV/s
Current density (A g-1)
Potential (V vs Ag/AgCl)
c
GO
5 mV/s
10 mV/s
25 mV/s
50 mV/s
Current density (A g-1)
Potential (V vs Ag/AgCl)
d
Ni(OH)2/GO
5 mV/s
10 mV/s
25 mV/s
50 mV/s
Current density (A g-1)
Potential (V vs Ag/AgCl)
e
Mix-Ni(OH)2/GO
5 mV/s
10 mV/s
25 mV/s
50 mV/s
Current density (A g-1)
Potential (V vs Ag/AgCl)
f
Ni(OH)2/GO
Mix Ni(OH)2/GO
Ni(OH)2
GO
Potential (V vs Ag/AgCl)
Time (s)

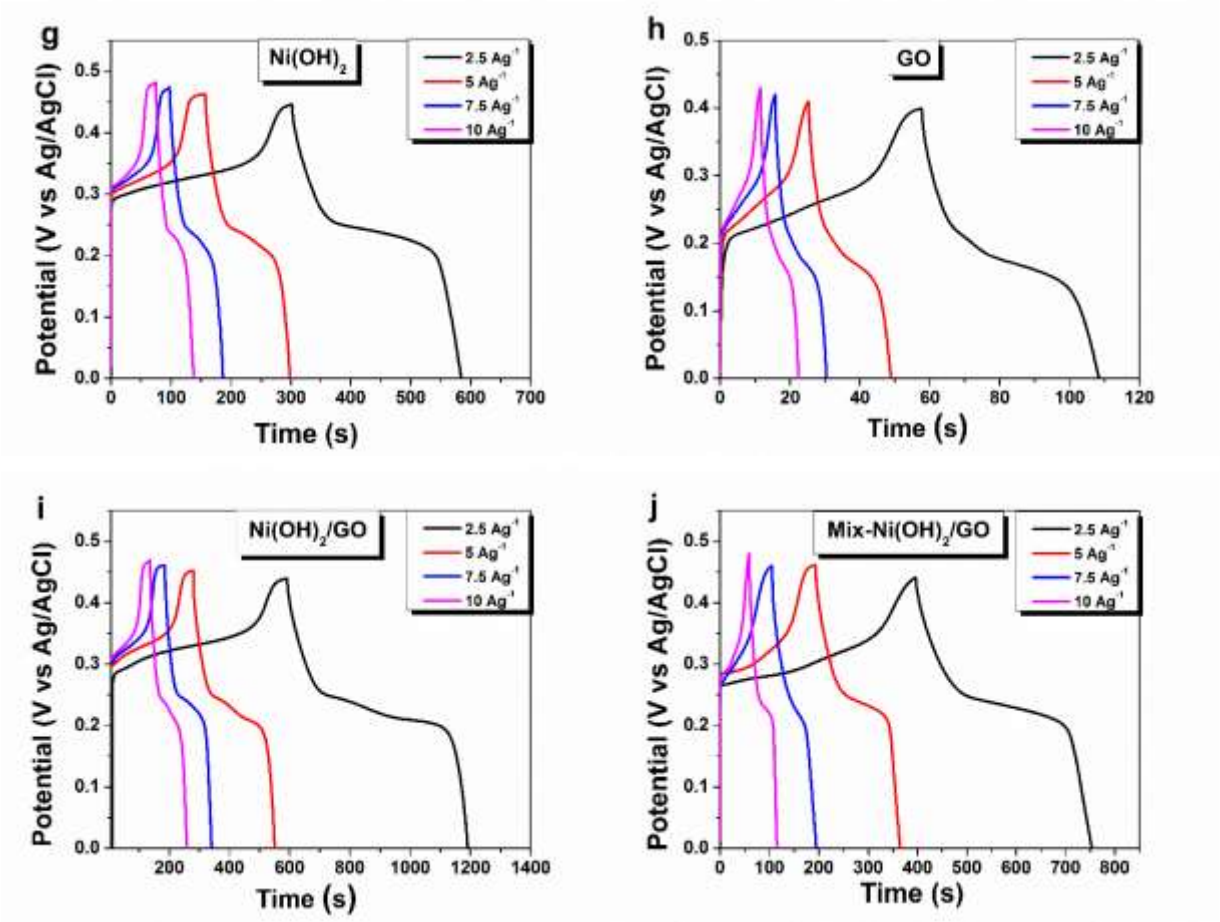

Fig. 9 CV curves of (a) pure $Ni(OH)_2$, GO, $Ni(OH)_2$/GO and Mix-Ni(OH)2/GO electrodes at 10 mVs^{-1}, (b-e) pure $Ni(OH)_2$, GO, $Ni(OH)_2$/GO and Mix-Ni(OH)2/GO electrodes at different scan rates respectively; CD curves of (f-i) pure $Ni(OH)_2$, GO, $Ni(OH)_2$/GO and Mix-Ni(OH)2/GO electrodes at different current densities respectively.

Fig. 9f shows CD curves comparing $Ni(OH)_2$, GO, $Ni(OH)_2$/GO, and Mix-$Ni(OH)_2$/GO electrodes at a current density of 2.5 A g^{-1}. The discharge time of the $Ni(OH)_2$/GO electrode is considerably longer than the other electrodes signifying a better discharge rate and subsequently an improved specific capacity/capacitance. This is in agreement with the CV curves in Fig. 9a.

It can be observed in Fig. 9g-j that CD curves for pure $Ni(OH)_2$, GO, $Ni(OH)_2$/GO and Mix-$Ni(OH)_2$/GO electrodes are not an ideal straight lines as a function of time as would be expected for EDLC. This signifies that a faradaic charge storage mechanism is occurring and this confirms

the redox activities observed in the CV curves. In addition high discharge time observed in the CD curve of $Ni(OH)_2$/GO at 2.5 A g^{-1} resulted to a higher specific capacity of $\sim$ 420 mA h g^{-1} and specific capacitance of ~ 3619 F g^{-1} compared to that of the pure $Ni(OH)_2$, GO, and Mix-Ni(OH)2/GO electrodes calculated using equations 2 and 3 respectively [41,42]:

$$Q = {It}/{m * 3.6} \quad (2)$$

Where *Q* is the discharge specific capacity (mA h g^{-1}), t is the discharge time (s), I is a current (mA), and m is the mass of active material (g).

$$C_s = \frac{2I_D}{V^2} \int V(t)dt \quad (3)$$

Where C_s is the discharge specific capacitance (F g^{-1}), t is the discharge time (s), I_D is a current density (A g^{-1}), and V is the applied potential (V).

The higher specific capacity and capacitance recorded for the $Ni(OH)_2$/GO electrode could be due to: (a) The increased in the specific surface area in $Ni(OH)_2$/GO composite due to the presence of GO which leads to providing more contact area with the electrolyte; (b) the extra specific capacity coming from the enriched oxygen-containing functional group of GO present in the composite, as well as increased wettability [13,39]; and (c) the good synergy between GO and $Ni(OH)_2$ which does not exist in the case of the Mix-$Ni(OH)_2$/GO.

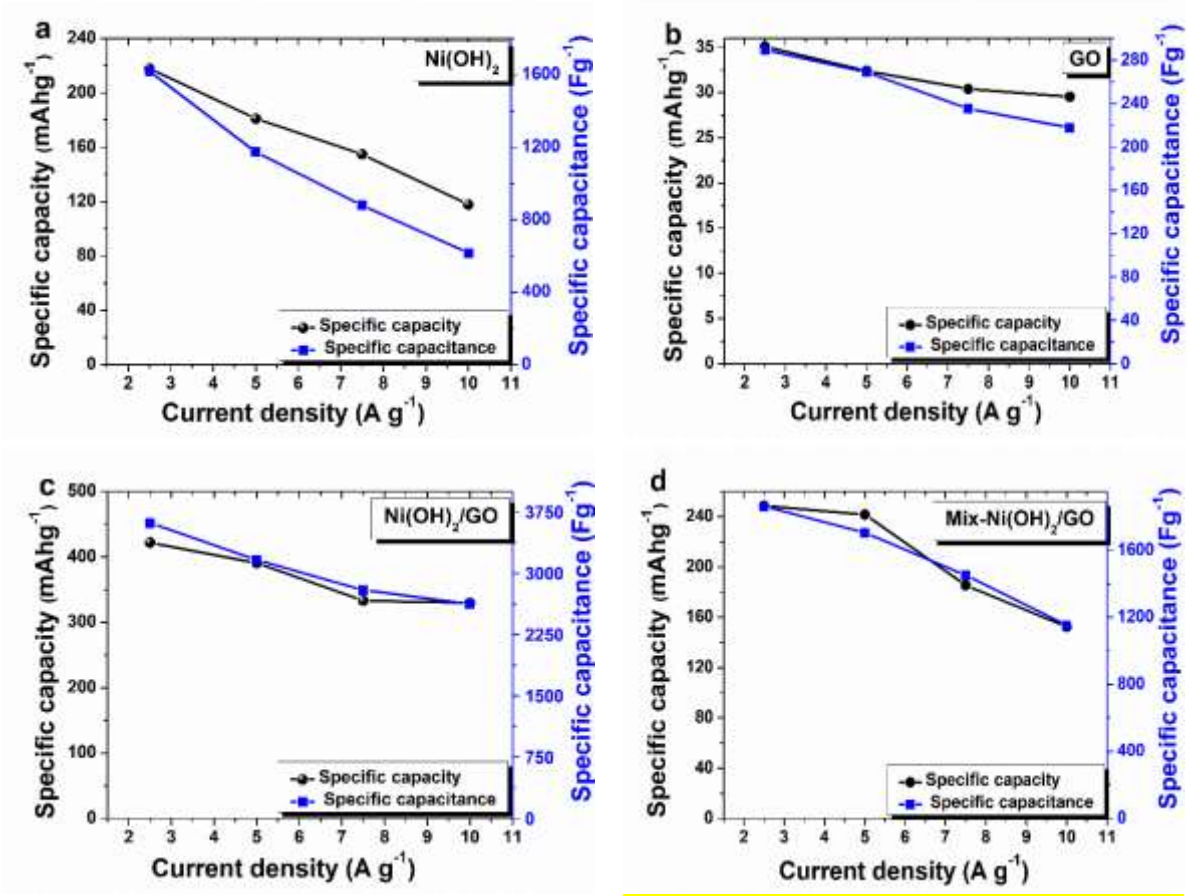

Fig. 10 Specific capacity/specific capacitance as a function of current density of (a) pure $Ni(OH)_2$, (b) GO, (c) $Ni(OH)_2$/GO (d) Mix-Ni(OH)2/GO.

Fig. 10a-d present plots of specific capacity/specific capacitance as a function of current density for $Ni(OH)_2$, GO, $Ni(OH)_2$/GO and Mix-Ni(OH)2/GO electrodes. High specific capacities/capacitances were recorded at low current densities, attributing to the higher accessibility of the electrolyte ions to the outer surface of the electrode material for the redox process. Whereas, the decrease in specific capacities for the pure $Ni(OH)_2$ and Mix-Ni(OH)2/GO with the increase in the current densities is as a result of the slow redox reaction, which is partly due to the low accessibility of the electrolyte ions to the outer surface of the active materials [4,43]. The rate capability of the electrodes is a vital characteristic for supercapacitor application. From Fig. 10b and 10c, the specific capacities/ capacitances of GO and $Ni(OH)_2$/GO

electrodes decrease very slowly as compared to that of the pure $Ni(OH)_2$ and Mix-$Ni(OH)_2$/GO (Fig. 10a and 10d). Furthermore, a good rate capability of ~78 % was demonstrated for $Ni(OH)_2$/GO at a high current density of 10 A g^{-1} (Fig. 10c). Moreover, compared with the previous literatures on supercapacitors from $Ni(OH)_2$-carbons based materials, our materials display higher specific capacitance and excellent rate capability as illustrated in Table 1.

Table 1. Electrochemical performance comparison of $Ni(OH)_2$-carbon based electrodes

Materials	Synthesis technique	Specific capacitance	Rate capability	References
hGN	Hydrothermal	1160 F g^{-1} at 5 A g^{-1}	54% (5-40 A g^{-1})	[19]
PGHS-$Ni(OH)_2$	Electrochemical deposition	1100 F g^{-1} at 4 A g^{-1}	72% (2-20 A g^{-1})	[44]
NG/$Ni(OH)_2$	Hydrothermal	1748 F g^{-1} at 0.5 A g^{-1}	80% (0.2-20 A g^{-1})	[18]
β-Ni(OH)2/GO/CNTs	Phase transformation	1815 F g^{-1} at 10 A g^{-1}	47% (2-20 A g^{-1})	[14]
GNiF	Extended filtration assisted	573 F g^{-1} at 0.2 A g^{-1}	72% (0.2-50 A g^{-1})	[45]
RGO-$Ni(OH)_2$	Two-step approach hydrothermal	1717 F g^{-1} at 0.5 A g^{-1}	55% (0.5-10 A g^{-1})	[5]
$Ni(OH)_2$/GF	Hydrothermal	2420 F g^{-1} at 1 A g^{-1}	21% (1-20 A g^{-1})	[4]
$Ni(OH)_2$/GNs	Hydrothermal	2260 F g^{-1} at 1 A g^{-1}	62% (1-10 A g^{-1})	[8]
Ag/$Ni(OH)_2$/3DG	Hydrothermal	2167 F g^{-1} at 10 A g^{-1}	65% (10-80 A g^{-1})	[46]
$Ni(OH)_2$	Solvothermal	1619 F g^{-1} at 2.5 A g^{-1}	54% (2.5-10 A g^{-1})	This work
$Ni(OH)_2$/GO	Solvothermal	3619 F g^{-1} at 2.5 A g^{-1}	78% (2.5-10 A g^{-1})	This work

Fig. 11a presents Nyquist plots of the pure $Ni(OH)_2$, GO, $Ni(OH)_2$/GO and Mix-$Ni(OH)_2$/GO electrodes. The Nyquist plots of $Ni(OH)_2$/GO and GO electrodes are found to have smaller partial semi-circular arcs at the high-frequency region, indicating lower charge transfer

resistance (R_{ct}) value in comparison to the one observed in $Ni(OH)_2$ and Mix-$Ni(OH)_2$/GO. R_{ct} is the resistance due to the transfer of charges between active materials and electrolyte ions. In addition, almost an ideal vertical line observed in the low-frequency region of GO and $Ni(OH)_2$/GO electrodes reveal an ideal capacitive behavior [43]. Solution resistance (R_S) also known as an equivalent series resistance, is defined as the sum of the resistance at electrolyte /electrode/current collector interfaces and can be deduced from the intercept of the Nyquist plot to the real axis. $Ni(OH)_2$/GO electrode is found to have smaller R_S of 0.69 Ω than $Ni(OH)_2$, GO and Mix-$Ni(OH)_2$/GO electrode with R_S values of 1.82 Ω, 0.96 Ω, and 0.71 Ω, respectively.

Cycling stability is very important to evaluate the electrochemical performance of the electrode material. Fig. 11b shows the capacity retention of $Ni(OH)_2$/GO electrode as a function of cycle number at 10 A g^{-1}, for 3000 cycles, with capacity retention of ~ 95% , this represents only 5% of capacity loss after 3000 cycles.

Fig. 11c and 11d display the Nyquist plots before and after cycling for the $Ni(OH)_2$/GO electrode. A slight change in R_S values is observed after 3000 charge-discharge cycles at 10 A g^{-1}. Nevertheless, more deviation from the vertical line is observed, indicating more leakage resistance after cycling. The partial semicircle at high frequency region slightly increased after cycling, resulting to an increase in R_{ct} value from 0.47 Ω to 1.26 Ω. Insets to Fig. 11c and 11d are the equivalent circuits after modeling with a (ZFIT) software. L is the inductance, R_{ct} is the charge transfer resistance, R_s is the solution resistance, R_L is the leakage resistance due to the Faradaic reaction, W is the Warburg which responsible for the ion diffusion within the active materials, Q_1 and Q_2 are the constant phase elements (CPEs) elements which are non-intuitive circuit elements that are used in place of a capacitance in the series circuit with the resistance.

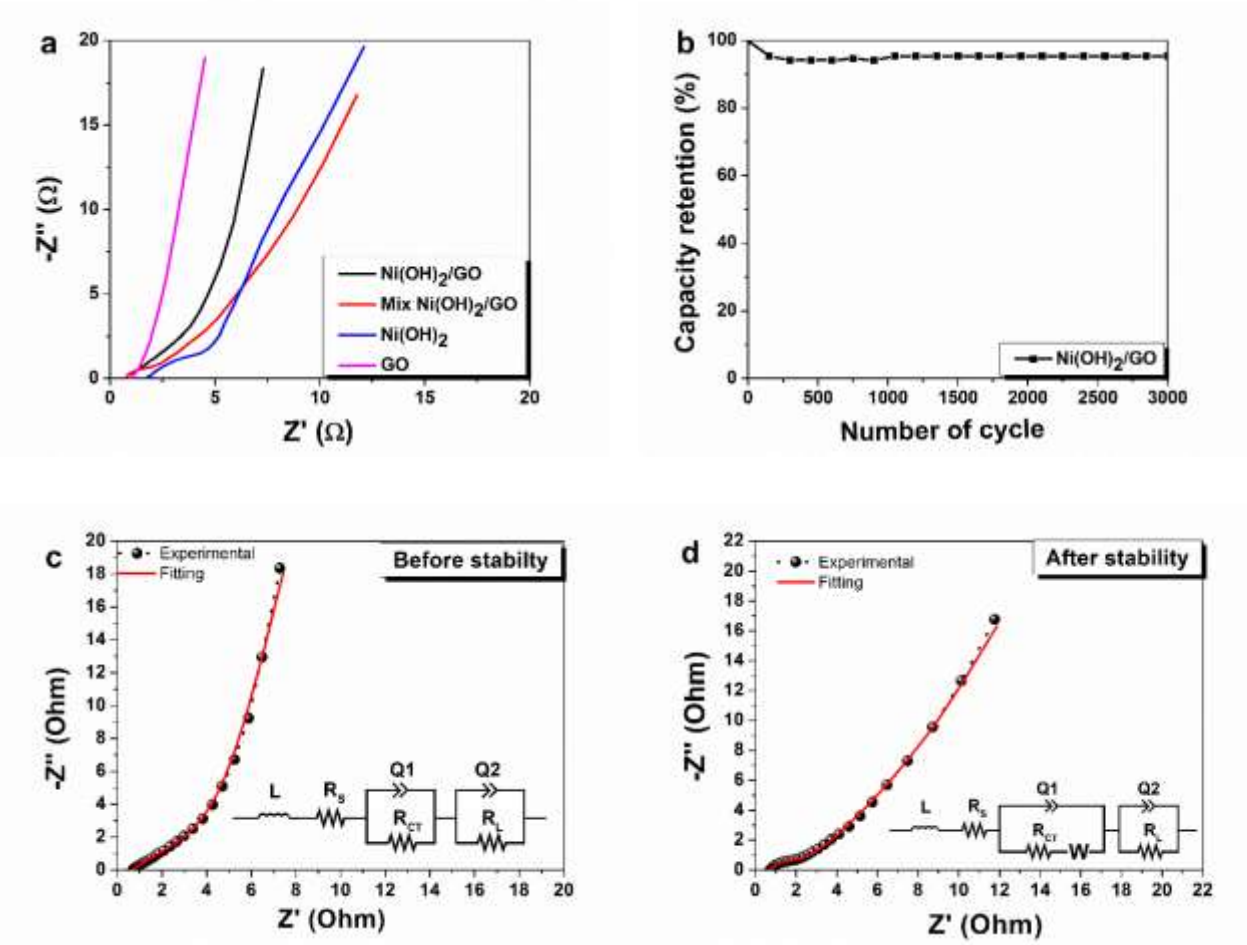

Fig. 11. EIS spectra of (a) Pure $Ni(OH)_2$, GO, $Ni(OH)_2$/GO and Mix-Ni(OH)2/GO electrodes, (b) Capacity retention of $Ni(OH)_2$/GO electrode after 3000 cycles at 10 A g^{-1}, (c-d) EIS spectra of $Ni(OH)_2$/GO electrode before and after cycling.

In Fig. 11c, the circuit consists of L connected in series with R_s, and Q_1 which is in parallel R_{ct}, and Q_2 in parallel R_L. Fig 11d contains L connected in series with R_s, Q_1 which is in parallel with the series connection of R_{ct} and W, and Q_2which is in parallel to R_L. The R_s and R_{ct} values of $Ni(OH)_2$/GO electrodes measured from (ZFIT) software before and after cycling are 0.686 Ω and 0.725 Ω, and 0.567 Ω and 1.24 Ω respectively, thus, implying that the models used for the fitting are within acceptable values with slight error margin.

Conclusion

In summary, spherical $Ni(OH)_2$/GO was synthesized using a surfactant free solvothermal procedure. The GO provides an ideal substrate for the growth of $Ni(OH)_2$, which results in the spherical $Ni(OH)_2$ serving as a barrier between GO sheets to successfully reduce the restacking of the GO sheets. Consequently, the $Ni(OH)_2$/GO electrode displays better electrochemical performance as compared with pure $Ni(OH)_2$ electrode with a specific capacity of ~ 420 $mAhg^{-1}$ which is close to the value of the theoretical capacity of $Ni(OH)_2$. In addition an excellent rate capability of ~78 % at current density of 10 A g^{-1}, with capacity retention of ~95 % after 3000 at 10 Ag^{-1} were observed. Hence, $Ni(OH)_2$/GO electrode has a potential as an electrode material for ECs application.

Acknowledgment

"This work is based on the research supported by the South African Research Chairs Initiative of the Department of Science and Technology and National Research Foundation of South Africa (Grant No 97994). Any opinion, finding and conclusion or recommendation expressed in this material is that of the author(s) and the NRF does not accept any liability in this regard". A. A. Khaleed acknowledges financial support from University of Pretoria and the NRF through SARChI in Carbon Technology and Materials for his Ph.D. study.

References

[1] C.-Y. Cao, W. Guo, Z.-M. Cui, W.-G. Song, W. Cai, Microwave-assisted gas/liquid interfacial synthesis of flowerlike NiO hollow nanosphere precursors and their application as supercapacitor electrodes, J. Mater. Chem. 21 (2011) 3204.

[2] A.S. Aricò, P. Bruce, B. Scrosati, J.-M. Tarascon, W. van Schalkwijk, Nanostructured materials for advanced energy conversion and storage devices, Nat. Mater. 4 (2005) 366–377.

[3] Y. Guo, J. Hu, L. Wan, Nanostructured materials for electrochemical energy conversion and storage devices, Adv. Mater. 20 (2008) 2878–2887.

[4] A.A. Khaleed, A. Bello, J.K. Dangbegnon, F.U. Ugbo, F. Barzegar, D.Y. Momodu, M. J. Madito, T. M. Masikhwa, O. Olaniyan, N. Manyala, A facile hydrothermal reflux synthesis of $Ni(OH)_2$/GF electrode for supercapacitor application, J. Mater. Sci. 51 (2016) 6041–6050.

[5] Y. Liu, R. Wang, X. Yan, Synergistic Effect between Ultra-Small Nickel Hydroxide Nanoparticles and Reduced Graphene Oxide sheets for the Application in High-Performance Asymmetric Supercapacitor., Sci. Rep. 5 (2015) 11095.

[6] C. Jiang, B. Zhao, J. Cheng, J. Li, H. Zhang, Z. Tang, J. Yang, Hydrothermal synthesis of $Ni(OH)_2$ nanoflakes on 3D graphene foam for high-performance supercapacitors, Electrochim. Acta. 173 (2015) 399–407.

[7] F. Barzegar, A.A. Khaleed, F.U. Ugbo, K.O. Oyeniran, D.Y. Momodu, A. Bello, J.K. Dangbegnon, N. Manyala, Cycling and floating performance of symmetric supercapacitor derived from coconut shell biomass, AIP Adv. 6 (2016) 115306.

[8] K. Wang, X. Zhang, X. Zhang, D. Chen, Q. Lin, A novel Ni(OH)2/graphene nanosheets electrode with high capacitance and excellent cycling stability for pseudocapacitors, J.

Power Sources. 333 (2016) 156–163.

[9] D.U. Lee, J. Fu, M.G. Park, H. Liu, A. Ghorbani Kashkooli, Z. Chen, Self-Assembled NiO/Ni(OH) $_2$ Nanoflakes as Active Material for High-Power and High-Energy Hybrid Rechargeable Battery, Nano Lett. 16 (2016) 1794–1802.

[10] J.-H. Zhong, A.-L. Wang, G.-R. Li, J.-W. Wang, Y.-N. Ou, Y.-X. Tong, Co_3O_4/$Ni(OH)_2$ composite mesoporous nanosheet networks as a promising electrode for supercapacitor applications, J. Mater. Chem. 22 (2012) 5656.

[11] J. Huang, P. Xu, D. Cao, X. Zhou, S. Yang, Y. Li, G. Wang, Asymmetric supercapacitors based on β-$Ni(OH)_2$ nanosheets and activated carbon with high energy density, J. Power Sources. 246 (2014) 371–376.

[12] T. Meng, Q.-Q. Xu, Y.-T. Li, X.-Y. Xing, C.-S. Li, T.-Z. Ren, Graphene Supported Ni-based Nanocomposites as Electrode Materials with High Capacitance, Electrochim. Acta. 155 (2015) 69–77.

[13] B. Xu, S. Yue, Z. Sui, X. Zhang, S. Hou, G. Cao, Y, Yang, What is the choice for supercapacitors: graphene or graphene oxide?, Energy Environ. Sci. 4 (2011) 2826.

[14] X. Ma, J. Liu, C. Liang, X. Gong, R. Che, A facile phase transformation method for the preparation of 3D flower-like β-$Ni(OH)_2$/GO/CNTs composite with excellent supercapacitor performance, J. Mater. Chem. A. 2 (2014) 12692.

[15] Y. Sun, Q. Wu, G. Shi, K.S. Novoselov, A.K. Geim, S. V. Morozov, et al., Graphene based new energy materials, Energy Environ. Sci. 4 (2011) 1113.

[16] J. Wei, Z. Zang, Y. Zhang, M. Wang, J. Du, X. Tang, Enhanced performance of light-controlled conductive switching in hybrid cuprous oxide/reduced graphene oxide (Cu_2O/rGO) nanocomposites, Opt. Lett. 42 (2017) 911.

[17] H. Wang, H.S. Casalongue, Y. Liang, H. Dai, $Ni(OH)_2$ nanoplates grown on graphene as advanced electrochemical pseudocapacitor materials., J. Am. Chem. Soc. 132 (2010) 7472–7.

[18] L. Mao, C. Guan, X. Huang, Q. Ke, Y. Zhang, J. Wang, 3D Graphene-Nickel Hydroxide Hydrogel Electrode for High-Performance Supercapacitor, Electrochim. Acta. 196 (2016) 653–660.

[19] S. Chen, J. Duan, Y. Tang, S. Zhang Qiao, Hybrid Hydrogels of Porous Graphene and Nickel Hydroxide as Advanced Supercapacitor Materials, Chem. - A Eur. J. 19 (2013) 7118–7124.

[20] K. Makgopa, P.M. Ejikeme, K.I. Ozoemena, Graphene oxide-modified nickel (II) tetra-aminophthalocyanine nanocomposites for high-power symmetric pseudocapacitor, Electrochim. Acta. 212 (2016) 876–882. doi:10.1016/j.electacta.2016.07.027.

[21] S.H. Aboutalebi, M.M. Gudarzi, Q. Bin Zheng, J.-K. Kim, Spontaneous Formation of Liquid Crystals in Ultralarge Graphene Oxide Dispersions, Adv. Funct. Mater. 21 (2011) 2978–2988.

[22] H. Feng, X. Wang, D. Wu, Fabrication of Spirocyclic Phosphazene Epoxy-Based Nanocomposites with Graphene via Exfoliation of Graphite Platelets and Thermal Curing for Enhancement of Mechanical and Conductive Properties, Ind. Eng. Chem. Res. 52

(2013) 10160–10171.

[23] D.S. Hall, D.J. Lockwood, C. Bock, B.R. MacDougall, Nickel hydroxides and related materials: a review of their structures, synthesis and properties, Proc. R. Soc. London A Math. Phys. Eng. Sci. 471 (2014).

[24] D.S. Hall, D.J. Lockwood, S. Poirier, C. Bock, B.R. MacDougall, Raman and Infrared Spectroscopy of α and β Phases of Thin Nickel Hydroxide Films Electrochemically Formed on Nickel, J. Phys. Chem. A. 116 (2012) 6771–6784.

[25] P.R. Jothi, K. Shanthi, R.R. Salunkhe, M. Pramanik, V. Malgras, S.M. Alshehri, Y. Yamauchi, Synthesis and Characterization of α--$NiMoO_4$ Nanorods for Supercapacitor -Application, Eur. J. Inorg. Chem. 2015 (2015) 3694–3699.

[26] Y. Gao, L. Mi, W. Wei, S. Cui, Z. Zheng, H. Hou, W. Chen, Double Metal Ions Synergistic Effect in Hierarchical Multiple Sulfide Microflowers for Enhanced Supercapacitor Performance, ACS Appl. Mater. Interfaces 7 (2015) 4311–4319

[27] A.C. Ferreira, A.P. Gonçalves, T.A. Gasche, A.M. Ferraria, A.M.B. do Rego, M.R. Correia, A.M. Bola, J.B. Branco, Partial oxidation of methane over bimetallic copper- and nickel-actinide oxides (Th, U), J. Alloys Compd. 497 (2010) 249–258.

[28] M. Hsiao, S. Liao, M. Yen, C. Teng, S. Lee, N. Pu, C. Wang, Y. Sung, M. Ger, C.M. Ma, M. Hsiao, Preparation and properties of a graphene reinforced nanocomposite conducting plate, J. Mater. Chem. 20 (2010) 8496.

[29] S. Ogawa, T. Yamada, S. Ishidzuka, A. Yoshigoe, M. Hasegawa, Y. Teraoka, Y. Takakoa,

Graphene Growth and Carbon Diffusion Process during Vacuum Heating on Cu (111)/ Al_2O_3 Substrates, Jpn. J. Appl. Phys. 52 (2013) 110122.

[30] H. Gao, Y. Wang, F. Xiao, C.B. Ching, H. Duan, Growth of Copper Nanocubes on Graphene Paper as Free-Standing Electrodes for Direct Hydrazine Fuel Cells, J. Phys. Chem. C. 116 (2012) 7719–7725.

[31] Y.-Z. Su, K. Xiao, N. Li, Z.-Q. Liu, S.-Z. Qiao, Amorphous $Ni(OH)_2$@ three-dimensional Ni core–shell nanostructures for high capacitance pseudocapacitors and asymmetric supercapacitors, J. Mater. Chem. A. 2 (2014) 13845.

[32] X. San, G. Wang, B. Liang, J. Ma, D. Meng, Y. Shen, Flower-like NiO hierarchical microspheres self-assembled with nanosheets: Surfactant-free solvothermal synthesis and their gas sensing properties, J. Alloys Compd. 636 (2015) 357–362.

[33] A. A.A. Khaleed, A. Bello, J.K. Dangbegnon, M.J. Madito, F.U. Ugbo, A. A. Akande, B. P. Dhonge, F. Barzegar, D. Y. Momodu, B. W. Mwakikunga, N. Manyala, Gas sensing study of hydrothermal reflux synthesized NiO/graphene foam electrode for CO sensing, J. Mater. Sci. 52 (2017) 2035–2044.

[34] A.A. Khaleed, A. Bello, J.K. Dangbegnon, D.Y. Momodu, M.J. Madito, F.U. Ugbo, A.A. Akande, B.P. Dhonge, F. Barzegar, O. Olaniyan, B.W. Mwakikunga, N. Manyala, Effect of activated carbon on the enhancement of CO sensing performance of NiO, J. Alloys Compd. 694 (2017) 155–162.

[35] C. Zhao, Q. Wang, H. Zhang, S. Passerini, X. Qian, Two-Dimensional Titanium

Carbide/RGO Composite for High-Performance Supercapacitors, ACS Appl. Mater. Interfaces. 8 (2016) 15661–15667.

[36] A. Singh, A. Chandra, Enhancing Specific Energy and Power in Asymmetric Supercapacitors - A Synergetic Strategy based on the Use of Redox Additive Electrolytes., Sci. Rep. 6 (2016) 25793.

[37] D. Han, P. Xu, X. Jing, J. Wang, P. Yang, Trisodium citrate assisted synthesis of hierarchical NiO nanospheres with improved supercapacitor performance, J. Power Sources. 235 (2013) 45–53.

[38] H. Cheng, A. Su, S. Li, S. Nguyen, L. Lu, Facile synthesis and advanced performance of Ni $(OH)_2$/CNTs nanoflake composites on supercapacitor applications, Chem. Phys. Lett. 601 (2014) 168–173.

[39] E. Frackowiak, Carbon materials for supercapacitor application, Phys. Chem. Chem. Phys. 9 (2007) 1774.

[40] J. Lee, T. Ahn, J. Kim, J. Ko, J. Kim, Nanosheets based mesoporous NiO microspherical structures via facile and template-free method for high performance supercapacitors, Electrochim. Acta. 56 (2011) 4849–4857.

[41] A. Laheäär, P. Przygocki, Q. Abbas, F. Béguin, Appropriate methods for evaluating the efficiency and capacitive behavior of different types of supercapacitors, 2015.

[42] B. Akinwolemiwa, C. Peng, G.Z. Chen, Redox Electrolytes in Supercapacitors, J. Electrochem. Soc. 162 (2015) A5054–A5059.

[43] W. Yang, Z. Gao, J. Wang, J. Ma, M. Zhang, L. Liu, Solvothermal one-step synthesis of Ni-Al layered double hydroxide/carbon nanotube/reduced graphene oxide sheet ternary nanocomposite with ultrahigh capacitance for supercapacitors., ACS Appl. Mater. Interfaces. 5 (2013) 5443–54. .

[44] F. Zhang, D. Zhu, X. Chen, X. Xu, Z. Yang, C. Zou, K. Yang, S. Huang, A nickel hydroxide-coated 3D porous graphene hollow sphere framework as a high performance electrode material for supercapacitors, Phys. Chem. Chem. Phys. 16 (2014) 4186.

[45] M. Li, Z. Tang, M. Leng, J. Xue, Flexible Solid-State Supercapacitor Based on Graphene-based Hybrid Films, Adv. Funct. Mater. 24 (2014) 7495–7502.

[46] W. Lan, Y. Sun, Y. Chen, J. Wang, G. Tang, W. Dou, Q. Su, E. Xie, Ultralight and flexible supercapacitor electrodes made from $Ni(OH)_2$ nanosheets doped with Ag nanoparticle/3D graphene composite, RSC Adv. 5 (2015) 20878–20883.